Planetary climate systems II

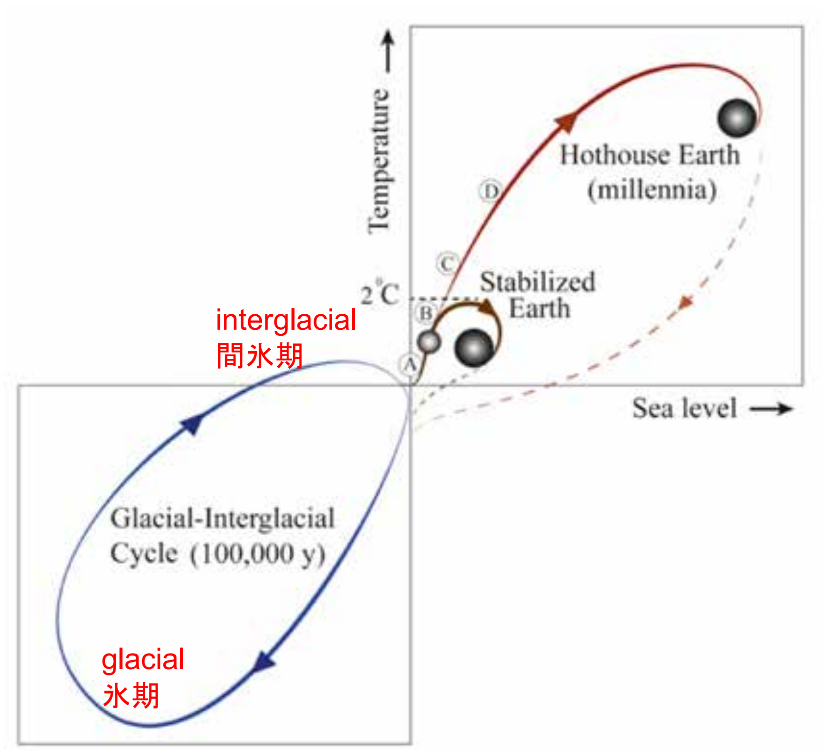

Steffen et al. (PNAS, 2018)

Milankovitch cycles on Mars and Earth

Table 12.10 The orbital elements of Mars and the Earth and their variability.

Parameter	Present Mars	Martian variability		Present Earth	Terrestrial variability	
		Range	Cycle (years)		Range	Cycle (years)
Obliquity (°)	25.19	0–85*	120 000**	23.45	22–24	41 000
Eccentricity	0.093	0–0.12	120 000***	0.017	0.01–0.04	100 000
Longitude of perihelion (°)	250	0–360	51 000	285	0–360	21 000

* Before ~10 Ma, obliquity variations are chaotic. While unpredictable at an exact time, statistically they would have varied between 0 and 85° (Laskar *et al.*, 2004; Touma and Wisdom, 1993).
** The amplitude of obliquity oscillation is modulated with a ~1.2 Myr period envelope.
*** The amplitude of eccentricity oscillation is modulated with a ~2.4 Myr period envelope.

Catling & Kasting 2017

Milankovitch cycle

from Wikipedia

low summer insolation in the northern high latitude
→ growth of ice sheets → glacial inception (ice age)

Precession 歳差

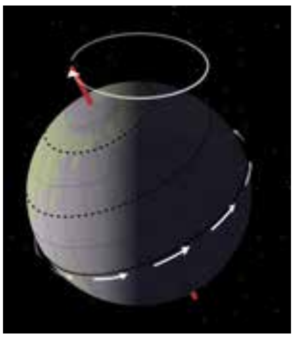

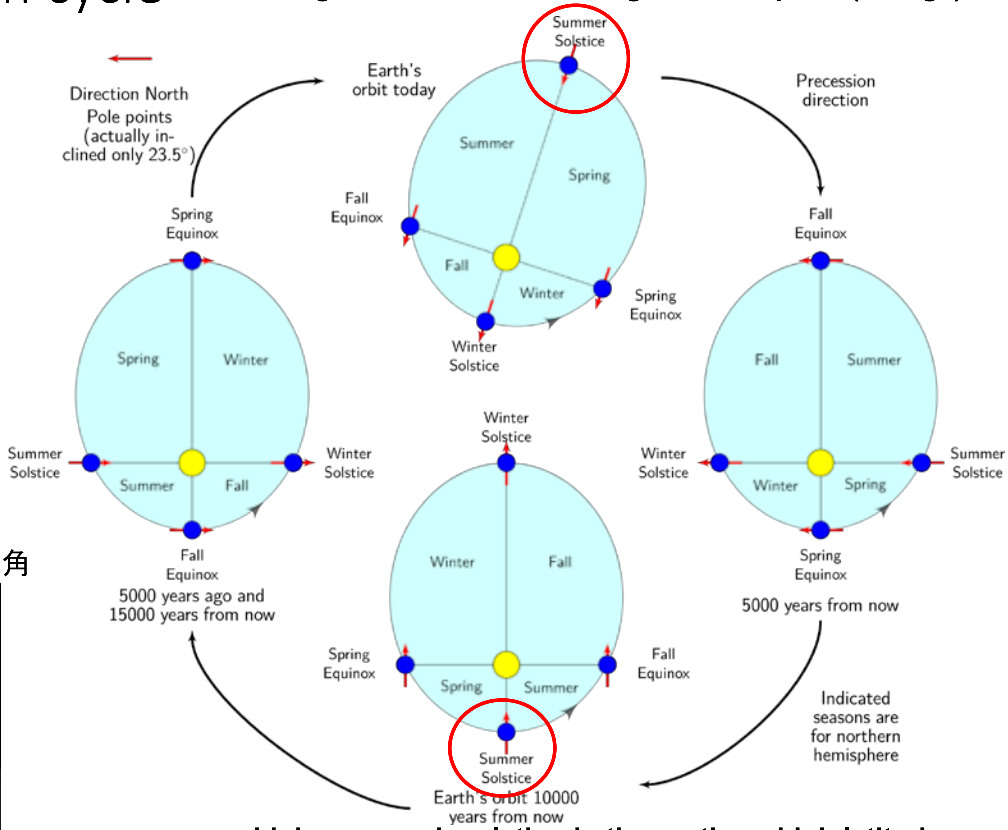

Obliquity 自転軸傾斜角

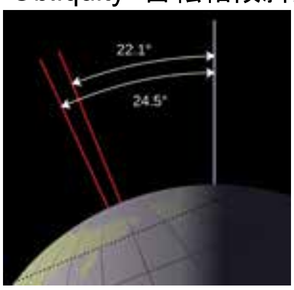

high summer insolation in the northern high latitude
→ decay of ice sheets → Interglacial (warm interval)

Glacial inception by CO_2 emission

Ganopolski et al. 2016, Nature

- Interglacials occur during periods of high summer insolation in the high latitudes of the Northern Hemisphere. (Milankovitch theory)
- In the past, a decrease in Northern Hemisphere insolation to below its present-day level always led to the end of interglacials and rapid growth of continental ice sheets.
- However, at present, although summer insolation at 65°N is close to its minimum, there is no evidence for the beginning of a new ice age.
- Glacial inceptions have occurred in the past under similar orbital configurations.

- The current interglacial would have ended if the CO_2 concentration had stayed at a level of about 240 parts per million (ppm), as was the case at the end of MIS19 (800 kyr BP). However, during the late Holocene (完新世：現代含む) before the beginning of the industrial era, the CO_2 concentration was about 280 ppm, leading to escape from glacial inception.
- It has been proposed that pre-industrial land-use at least partly contributed to the high Holocene CO_2 level, but the magnitude of this contribution is very uncertain.

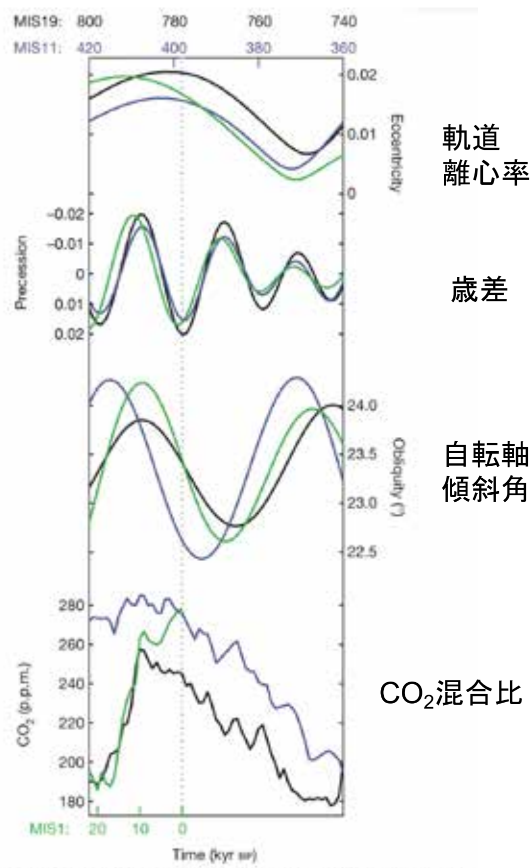

Figure 1 | Orbital parameters. Comparison of Earth's orbital parameters and CO_2 concentrations for MIS1 (green), MIS11 (blue) and MIS19 (black). The vertical dashed line corresponds to the present day for MIS1 and the minima of the precessional component of insolation for MIS11 and MIS19.

Future ?

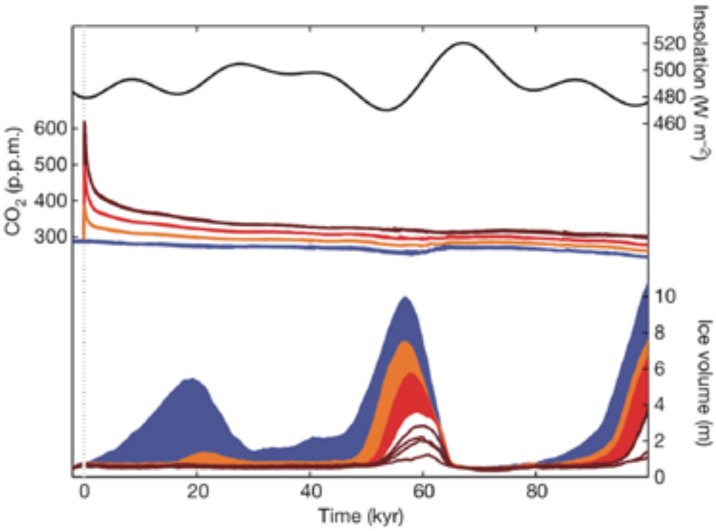

Figure 4 | The next glacial inception. The top panel shows the temporal evolution of the maximum summer insolation at 65° N. The middle panel shows the simulated CO_2 concentration during the next 100,000 years for different cumulative CO_2 emission scenarios: 0 Gt C anthropogenic emissions (blue), 500 Gt C (orange), 1,000 Gt C (red) and 1,500 Gt C (dark red line). The bottom panel shows simulated ice volume corresponding to the different CO_2 emission scenarios. Individual simulations are shown for the 1,500 Gt C scenario; for the other scenarios, the range is given as shading.

- For a total of 1,000 Gt carbon cumulative emissions, which is only double the present-day value, the probability of glacial inception during the next 100,000 years is notably reduced, and under cumulative emissions of 1,500 Gt C, glacial inception is very unlikely within the entire 100,000 years.
- Cumulative carbon emission will exceed 1,000 Gt in the twenty-first century, suggesting that anthropogenic interference will make the initiation of the next ice age impossible.

Mars

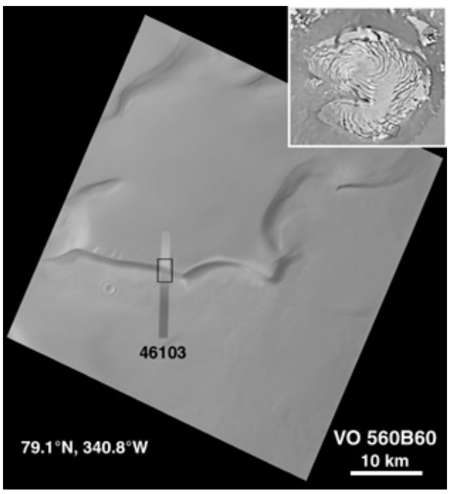

Polar cap deposits

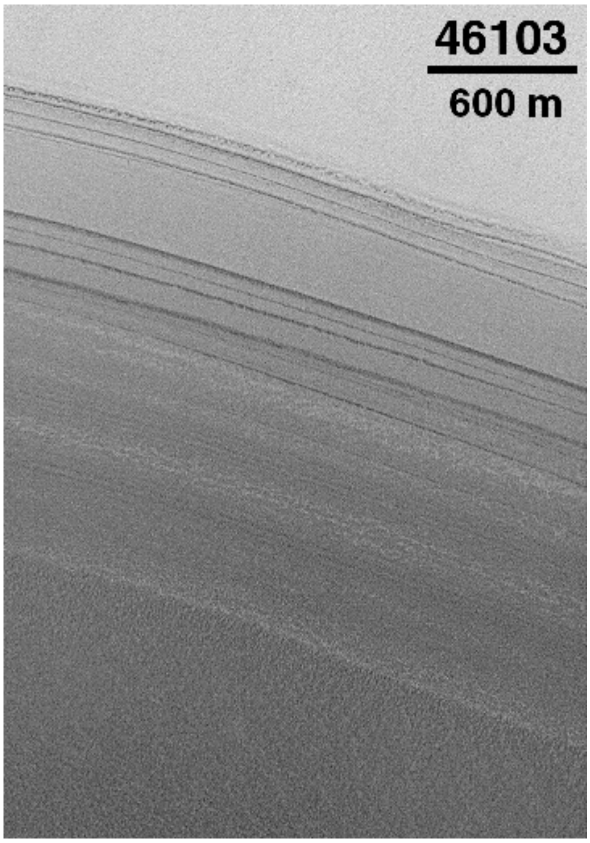

recurrent slope lineae

- transition between different climate regimes ?

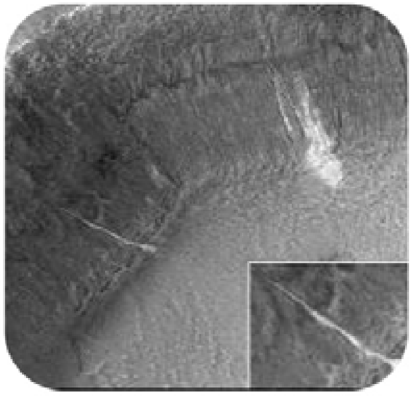

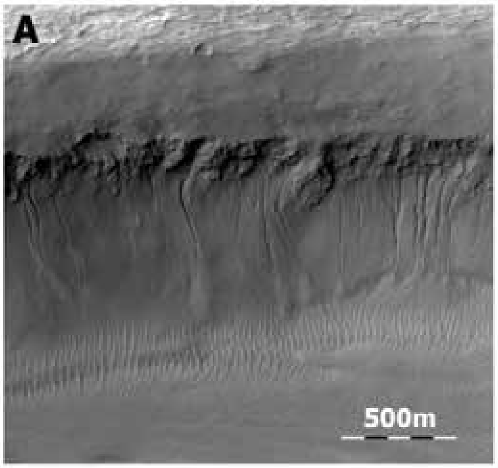

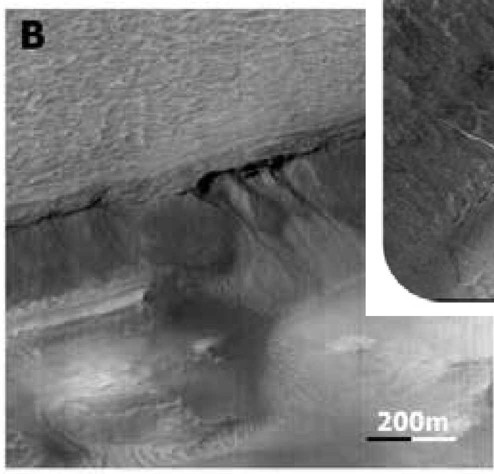

Subsurface ice

Mars Odyssey
Neutron Spectrometer (NS) and High-Energy Neutron Detector (HEND)

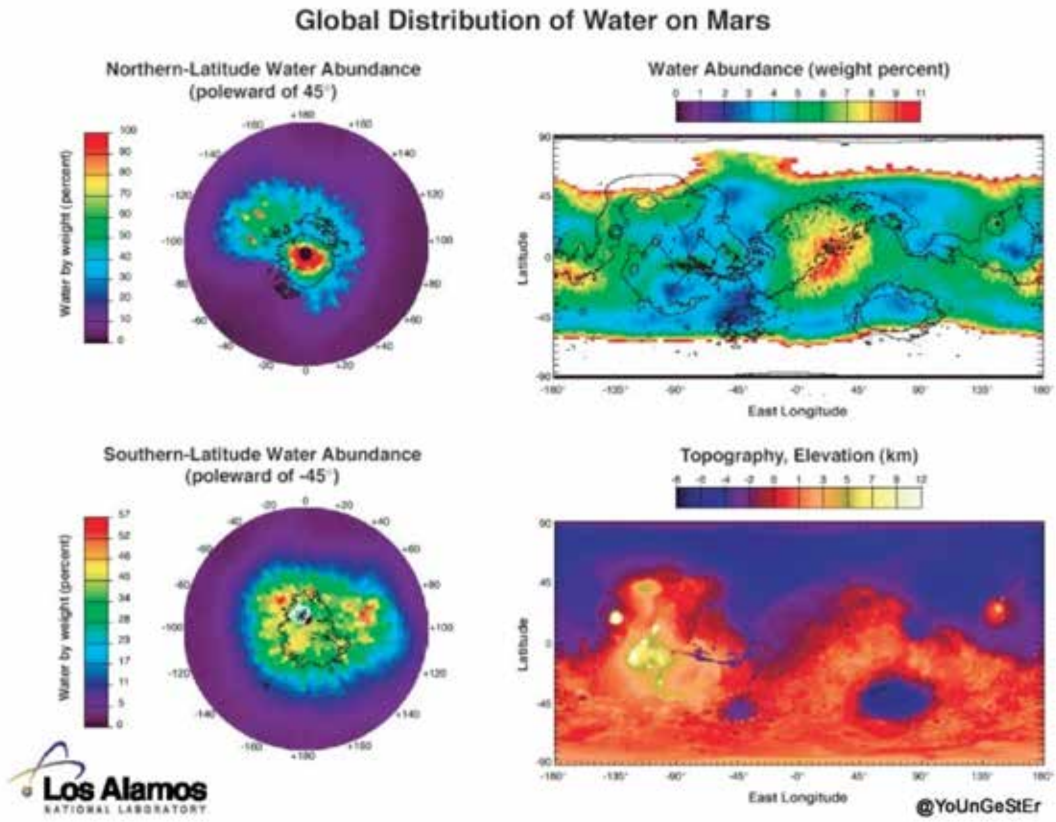

Schorghofer and Aharonson (2005)

Comparison with models

Near equilibrium at high latitudes ?

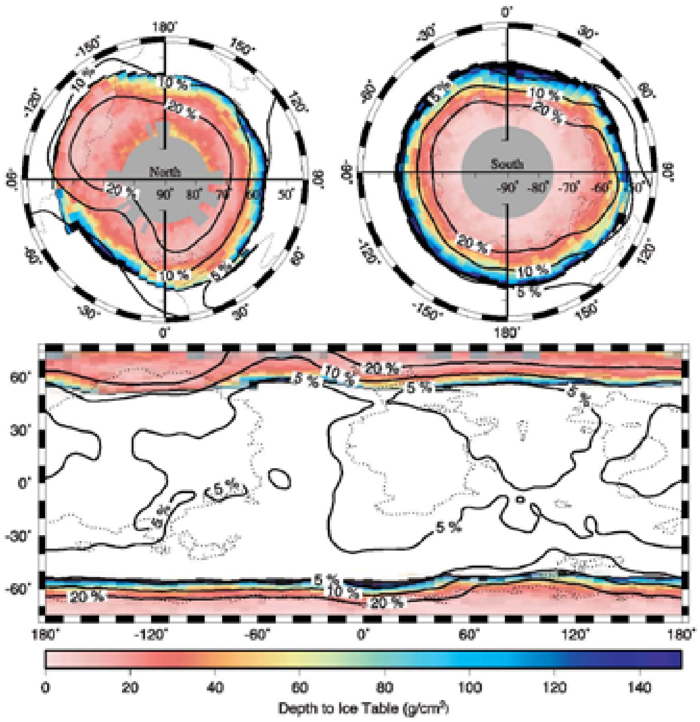

Figure 8. Color indicates depth to the ice table in g cm^{-2} when ice is in equilibrium with the atmospheric water vapor. Ground ice is unstable in the white area. Black segments indicate finite burial depths larger than 150 g cm^{-2}. Missing data points are shown in gray. Assumed volume fraction of ice is 40%, but the geographic boundary between icy and ice-free soil is independent of the ice fraction. Solid contours indicate water-equivalent hydrogen content in percent determined from neutron spectroscopy [*Feldman et al.*, 2004]. The dotted lines are 200 J m^{-2}K^{-1}s$^{-1/2}$ contours of thermal inertia.

色： 大気中の水蒸気との平衡状態を仮定して計算される氷床までの深さ

実線： 中性子分光観測から見積もられた水含有量

Permanent CO_2 cap at the South pole

青いところにCO_2氷　　　青いところにH_2O氷

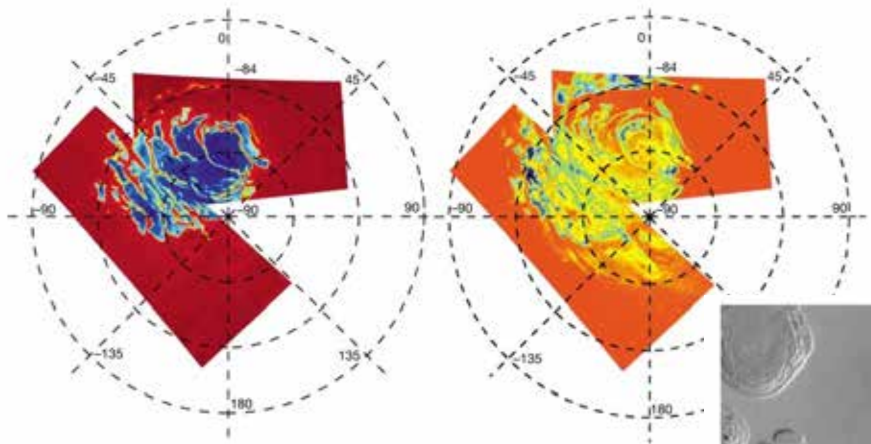

Figure 1 Global maps of CO_2 and H_2O ices at the south pole of Mars. Left, the CO_2-ice absorption feature is scaled from blue (deep) to brown (CO_2-ice-free areas); right, mapping of the H_2O ice, from blue (deep absorption) to red (ice-free). Comparison shows that the H_2O-ice areas extend far beyond the CO_2 isolated units tens of kilometres wide.

Bibring et al. (2004)

CO_2残存極冠のおかげで残存H_2O氷も存在か

浸食されつつある残存CO2極冠の一部

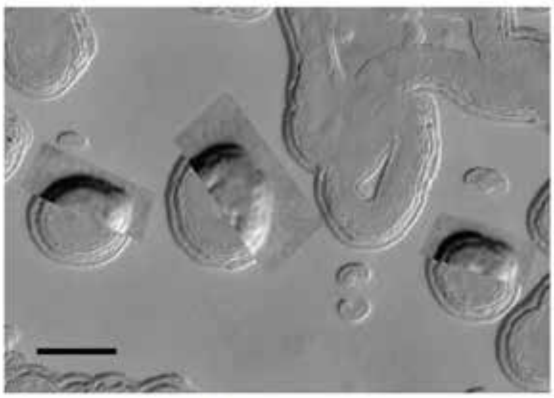

Fig. 8. Three year changes in unit B. Registered clips from MOC image E11-01220 superposed on HiRISE image PSP_004744_0870. Note that the three year change includes one or two ridges interior to the present depression edge. Illumination in MOC images from upper left, in HiRISE more from the left. MOC L_s = 286°, HiRISE L_s = 287°. Scale bar 50 m. Centered at 86.9°S, 89.4°W.

Milankovitch cycles on Mars and Earth

Table 12.10 The orbital elements of Mars and the Earth and their variability.

		Martian variability			Terrestrial variability	
Parameter	Present Mars	Range	Cycle (years)	Present Earth	Range	Cycle (years)
Obliquity (°)	25.19	0–85*	120 000**	23.45	22–24	41 000
Eccentricity	0.093	0–0.12	120 000***	0.017	0.01–0.04	100 000
Longitude of perihelion (°)	250	0–360	51 000	285	0–360	21 000

* Before ~10 Ma, obliquity variations are chaotic. While unpredictable at an exact time, statistically they would have varied between 0 and 85° (Laskar *et al.*, 2004; Touma and Wisdom, 1993).
** The amplitude of obliquity oscillation is modulated with a ~1.2 Myr period envelope.
*** The amplitude of eccentricity oscillation is modulated with a ~2.4 Myr period envelope.

Catling & Kasting 2017

Milankovitch cycles on Mars

自転軸傾斜角

軌道離心率

北極域の夏至の日射

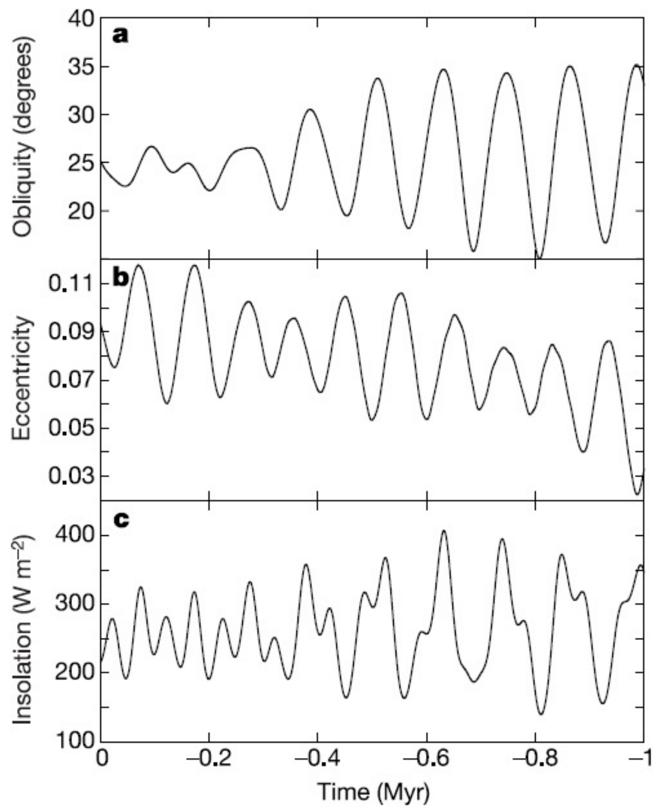

Laskar et al. (2002)

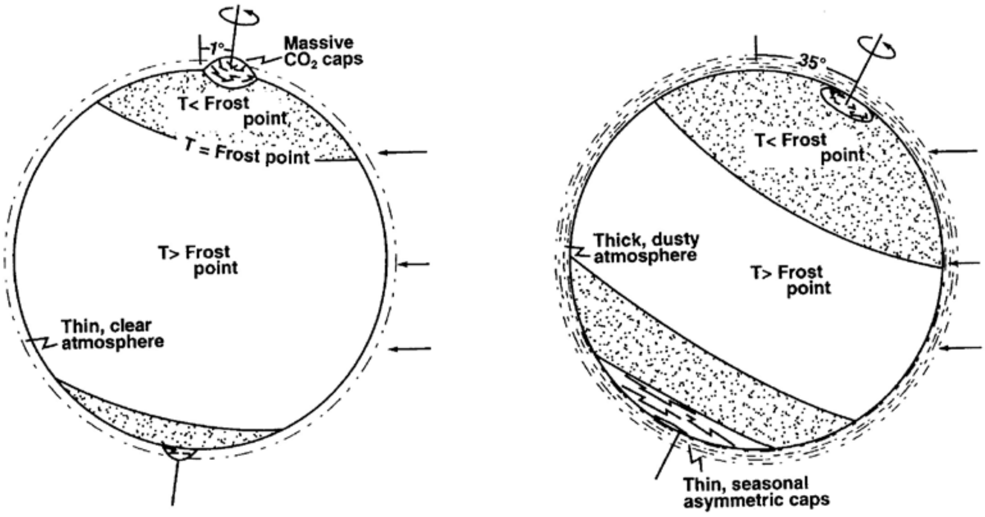

- low obliquity → cold pole → massive polar cap → dry atmosphere → retreat of ice sheet

- high obliquity → warm pole → thin polar cap → moist atmosphere → growth of ice sheet, ice accumulation in the tropics

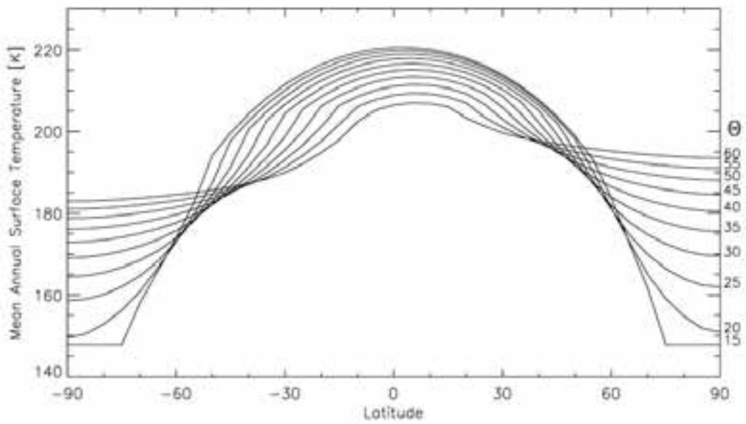

Figure 3. Mean annual surface temperature for a range of obliquities. The eccentricity is 0.12, and the L_S at which perihelion occurs is 270, corresponding to southern summer. A thermal inertia of 250 J m^{-2} s$^{-1/2}$ K^{-1}, an albedo of 0.25, a surface pressure of 600 Pa, and an infrared dust opacity of 0.1 are assumed. Discontinuities in the slope of each curve are due to the effects of seasonal CO_2 frost.

Mellon & Phillips (2001)

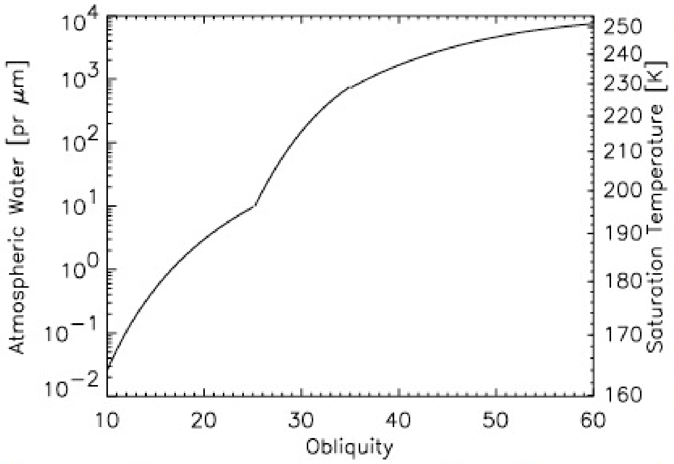

Buried glaciers

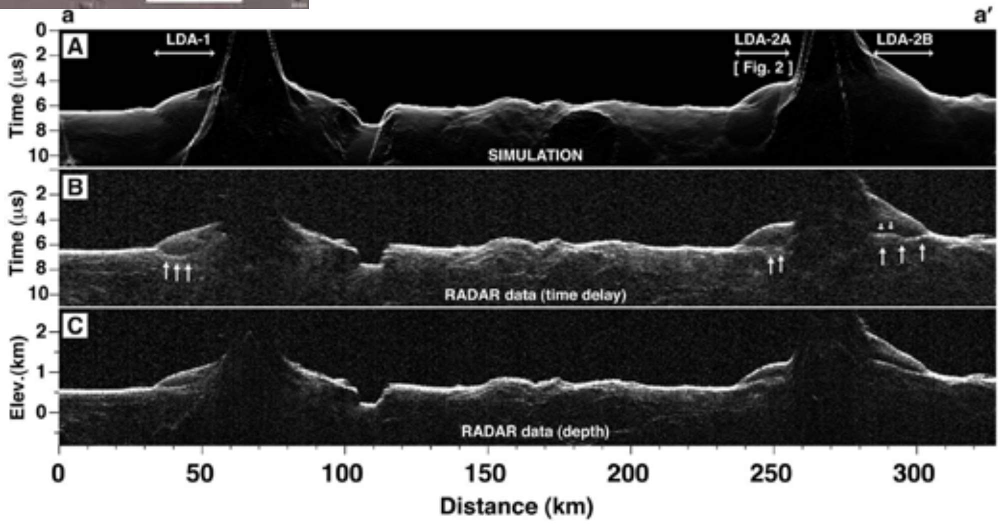

Formation of glaciers on Mars by atmospheric precipitation at high obliquity Forget et al. (2006)

- The model predicts ice accumulation in regions where glacier landforms are observed, on the western flanks of the great volcanoes and in the eastern Hellas region

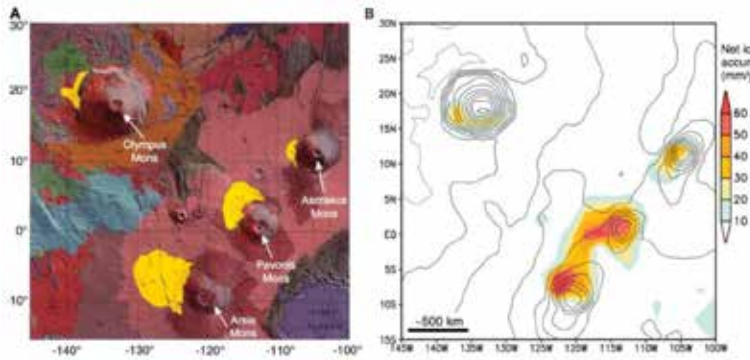

Fig. 1. (A) Geologic map modified from (30) of the Tharsis region showing the location of fan-shaped deposits of Amazonian age (yellow) located on the northwest slopes of the Tharsis Montes and Olympus Mons. (B) Net surface water ice accumulation in the Tharsis region simulated with 45° obliquity and assuming that surface water ice is present on the northern polar cap. Superimposed Mars Orbiter Laser Altimeter (MOLA) topography contours are at 2000-m intervals. (C) Same as (B) but for the Elysium Mons region. Outside the Tharsis and Elysium areas, no net ice accumulation is predicted.

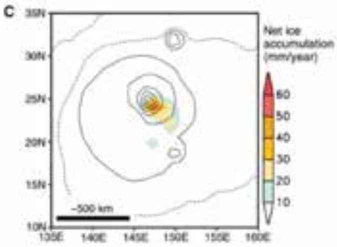

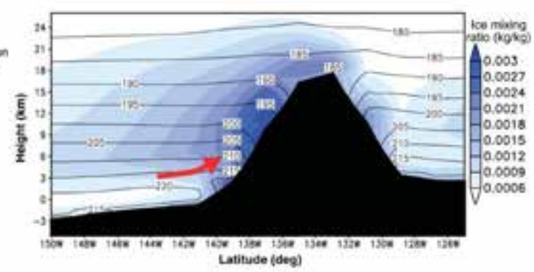

Fig. 3. Cross section of Olympus Mons along the 16°N latitude showing the mean atmospheric ice mass mixing ratio (shaded blue) and the atmospheric temperature (contour, K) averaged over the period of ice accumulation Ls = 125° to 155° (northern summer). The strong northwesterly winds induce adiabatic cooling on the flank of the volcanoes and atmospheric condensation and precipitation.

Seasons of Mars

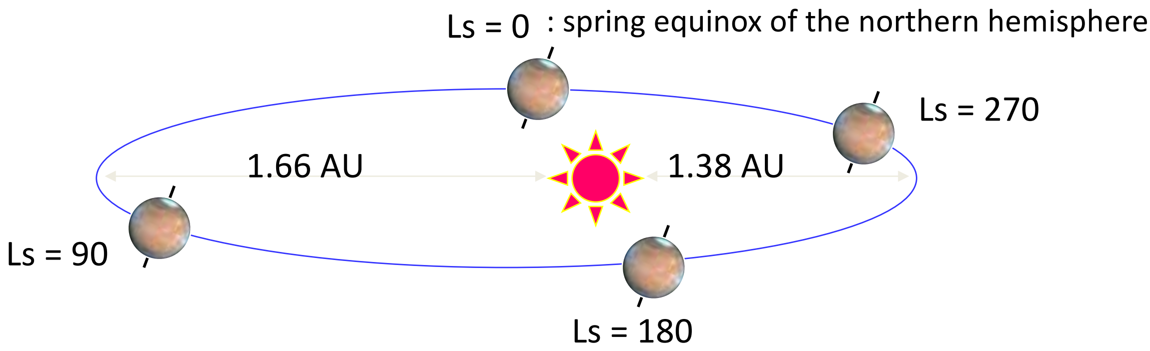

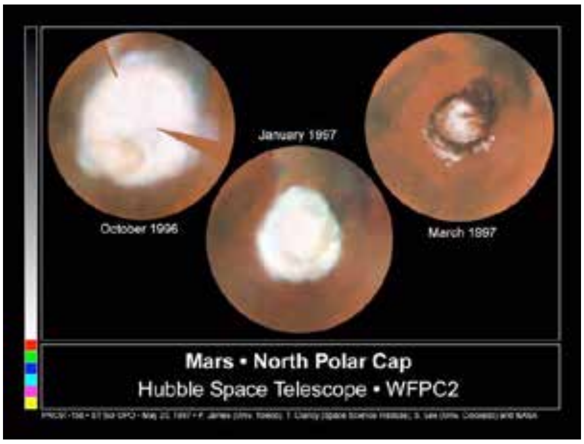

- 火星は公転軌道の離心率が大きいため季節変化が著しく南北非対称
- 南半球の夏に太陽までの距離が近くなる

Water transport by Hadley circulation

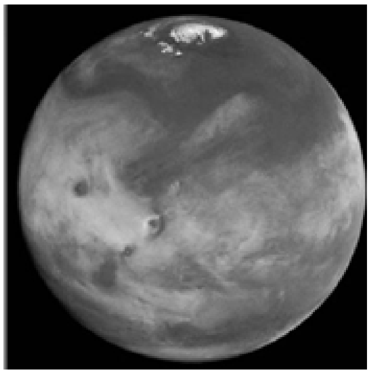

- Warmer southern summer than northern favors net northward transport of water.

Distribution of H_2O in a Mars GCM

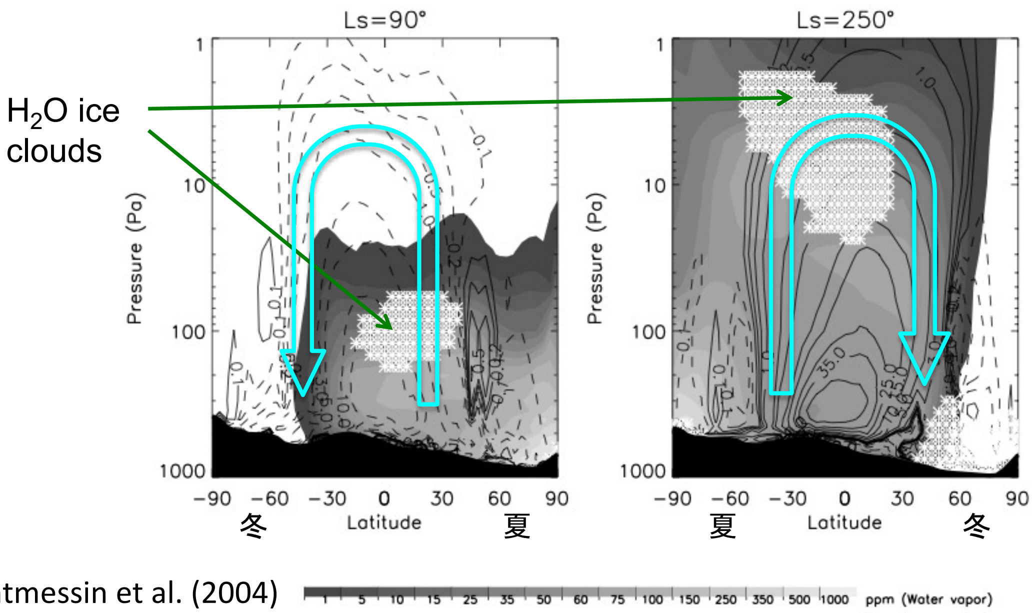

Montmessin et al. (2004)

Seasonal variation of dust, clouds, and H_2O vapor observed by an infrared spectrometer (TES) on Mars Global Surveyor

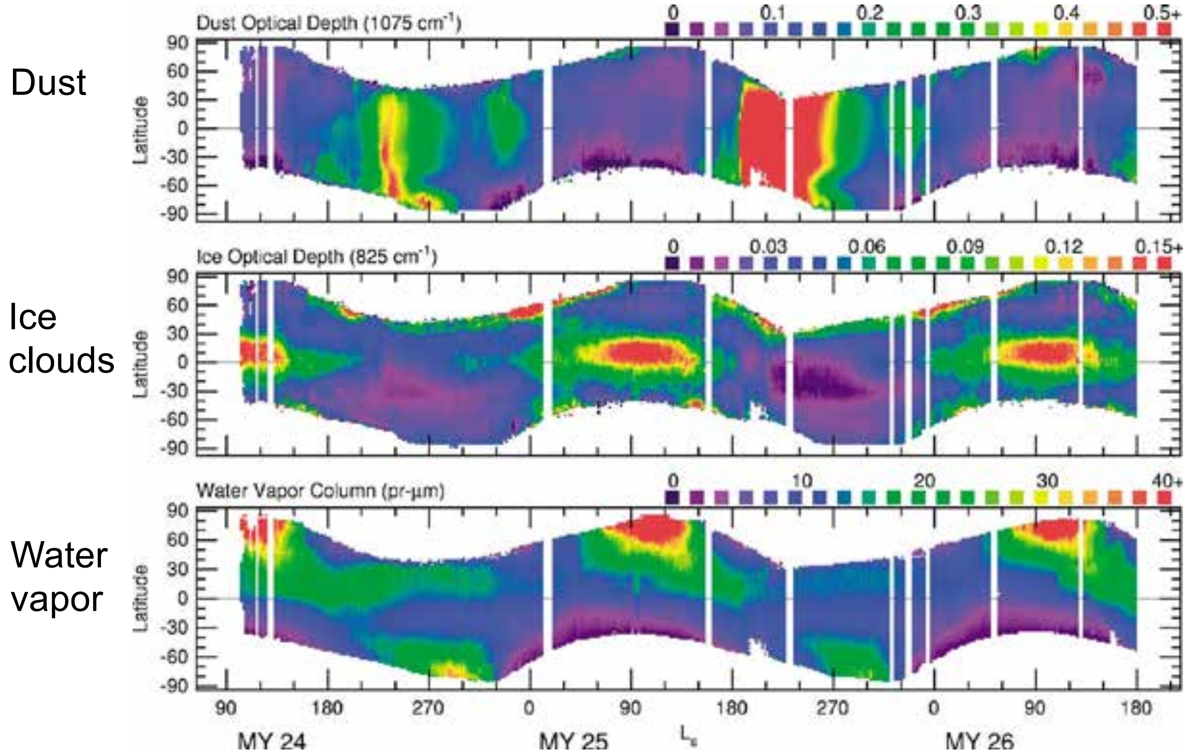

Smith, Icarus 167 (2004) 148–165

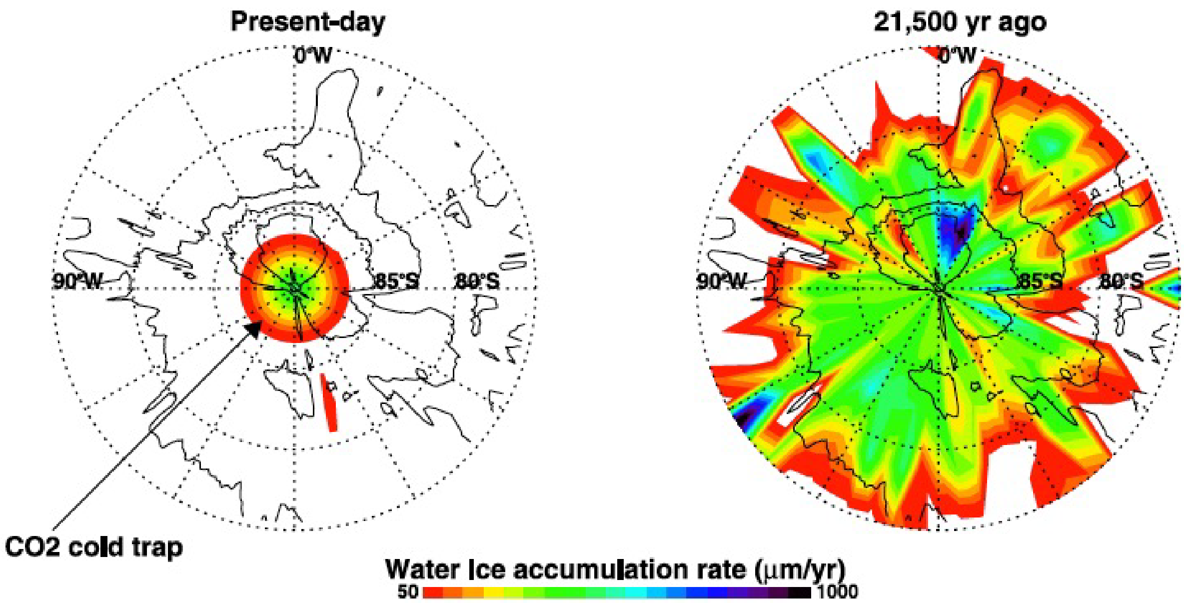

Figure 5. A comparison of water ice accumulation rates predicted by the model in the south polar region for the two perihelion configurations. Present-day map shows net accumulation only at the south pole itself (equivalent to 1 grid point in the model) where the prescription of a CO_2 cold trap forces a local and permanent deposition of water ice. In the reversed perihelion simulation (Figure 5, right), the CO_2 cold trap has been removed and the pattern of accumulation is only controlled by a precipitation versus sublimation positive balance on an annual average.

Supersaturation of water vapor on Mars

SPICAM on Mars Express (Maltagliati et al. 2011)

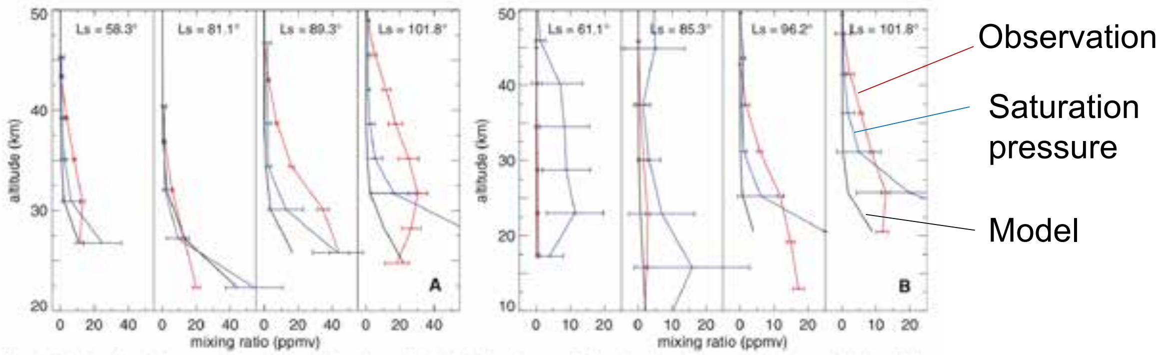

Fig. 2. Selection of typical water vapor volume–mixing ratio profiles in the (**A**) northern and (**B**) southern hemisphere. Black curve, modeled profile by the LMD-GCM; red curve, the retrieved SPICAM results; blue curve, saturation water vapor–mixing ratio. Supersaturation exists where the red values are greater than the blue ones.

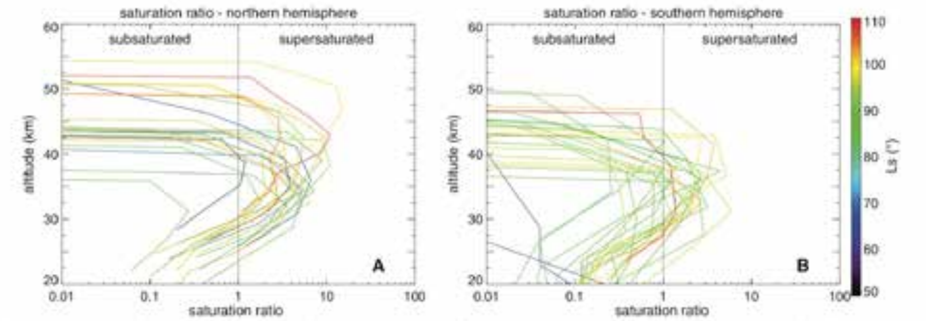

Fig. 3. Saturation ratio for all orbits of the campaign. (**A**) Northern hemisphere. (**B**) Southern hemisphere. The vertical line marks the value of 1, which corresponds to the saturated state.

Vertical distribution of water vapor on Mars during the course of a Mars year

Shaposhnikov et al. (2019)

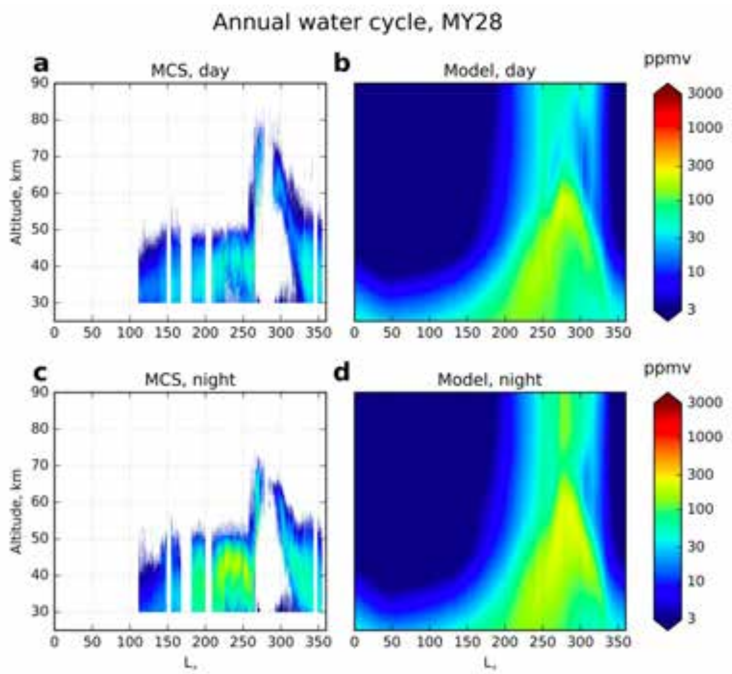

Figure 4. Vertical distribution of the total water (vapor+ice) content derived from the Mars Climate Sounder (MCS) measurements (left column) [*Heavens et al.*, 2018] and simulated with the MPI-MGCM (right column) for the MY28: for the day side (~15:00 local time, upper row) and night side (03:00 local time, lower row). In all panels, the values were averaged over longitudes and latitudes. In the simulations, the averaging over 14:00–16:00 and 02:00–04:00 local times was performed.

$H_2O \rightarrow H, H_2$

Nair et al. (1994)

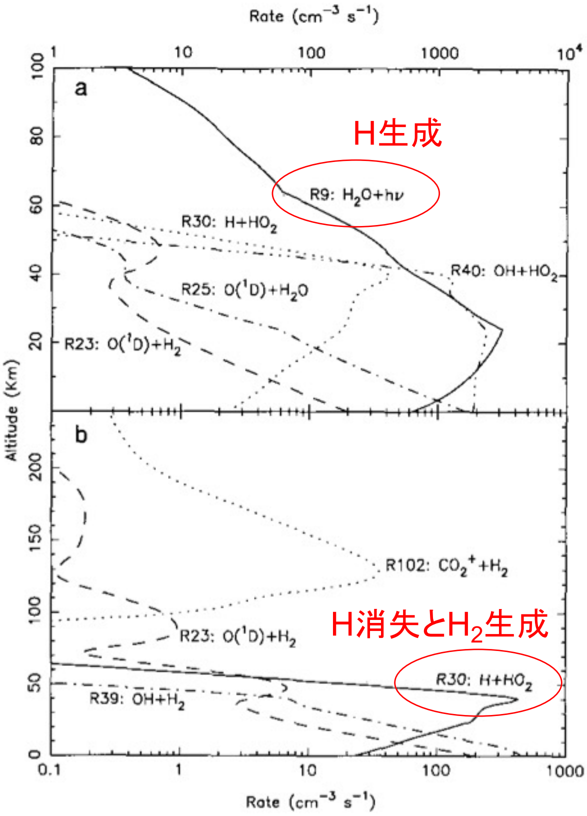

FIG. 5. (a) Production and loss rates for HO_x. (b) Production and loss rates for H_2.

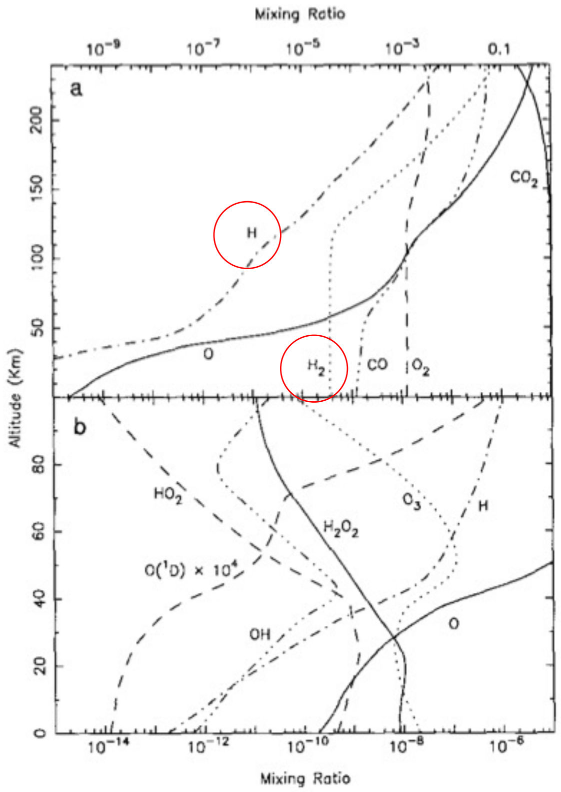

FIG. 3. Altitude vs mixing ratio profiles for the (a) major CHO and (b) HO_x and O_x species in our standard model. The integrated water abundance is 8.8 pr μm.

Nair et al. (1994)

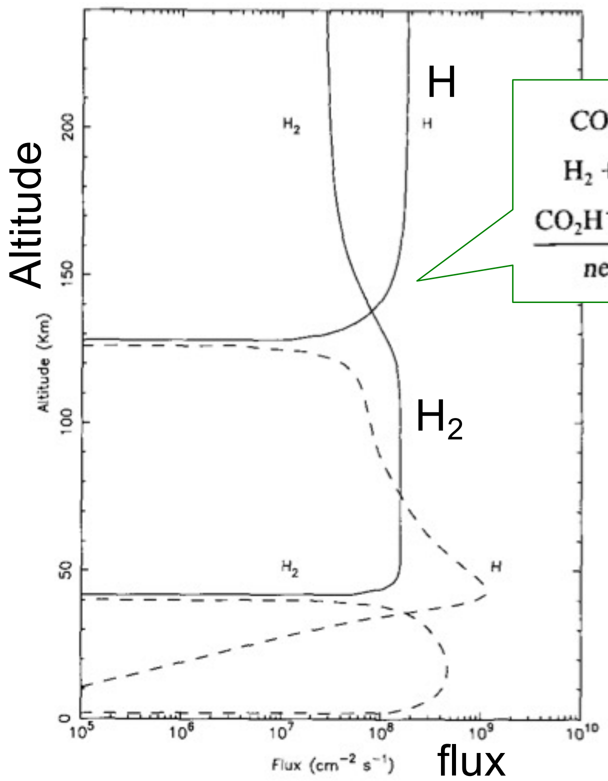

$$CO_2 + h\nu \rightarrow CO_2^+ + e^-$$
$$H_2 + CO_2^+ \rightarrow CO_2H^+ + H$$
$$CO_2H^+ + e^- \rightarrow CO_2 + H$$
$$\text{net} \quad H_2 \rightarrow 2H$$

- 高度数十kmでH_2Oは光解離
- 高度50-130kmでは主にH_2として輸送
- その上ではHとして輸送、散逸

FIG. 10. Computed fluxes of H and H_2. The solid lines indicate upward fluxes while the dashed lines indicate downward fluxes.

実線：上向きフラックス
波線：下向きフラックス

H_2SO_4 clouds of Venus

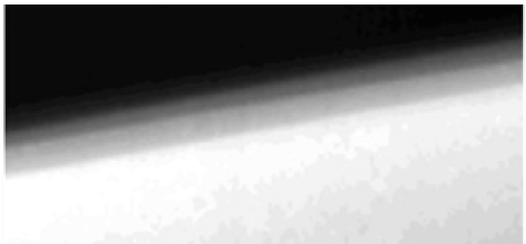

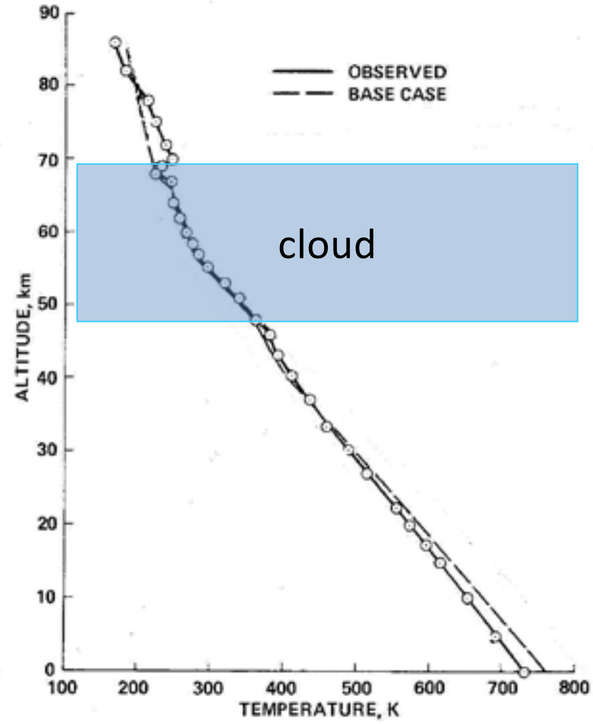

Fig. 2. Comparison between the observed temperature structure of Venus' lower atmosphere and that of several models, which are described in the main text.

- Solar energy flux reaching the Venus surface ($17 W/m^2$) is much less than that of the Earth ($168 W/m^2$).
- Greenhouse effect of massive CO_2 and small amount of H_2O explains the high temperature.

Pollack et al. (1980)

Variability of SO_2 above clouds

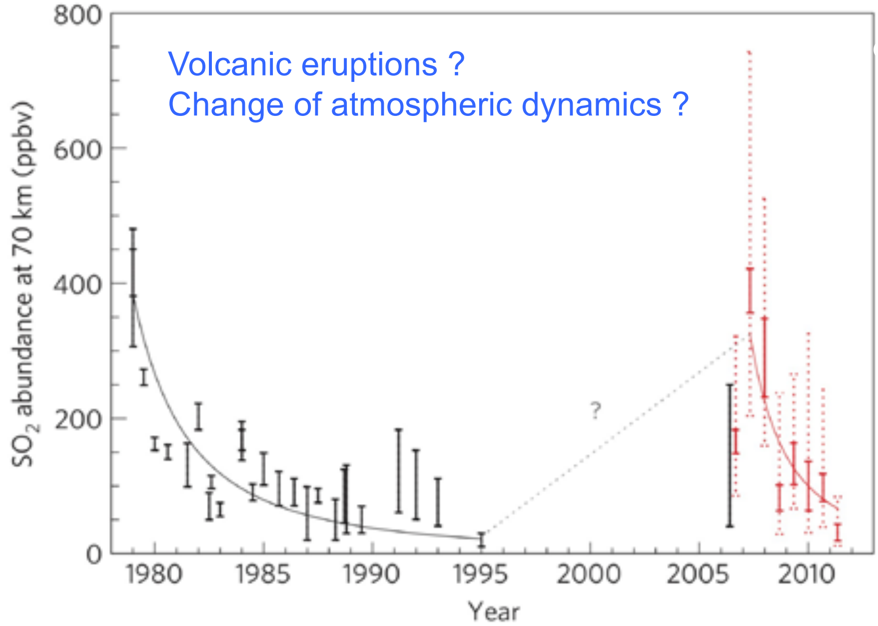

Marcq et al. (2013)

Figure 3 | More than thirty years of SO_2 measurements at Venus's cloud top. Black stands for previously published measurements[26]. Red stands for the 8-month moving average of the retrievals also shown in Fig. 1. Solid red error bars represent 1σ random uncertainty, and dotted red error bars represent measurement dispersion in each temporal bin.

Correlation between UV contrast and SO_2 density ? (Lee et al. 2015)

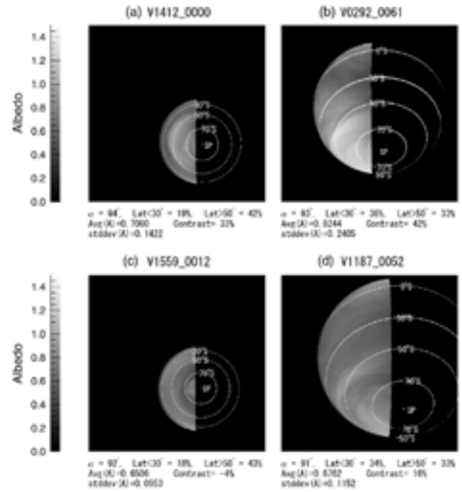

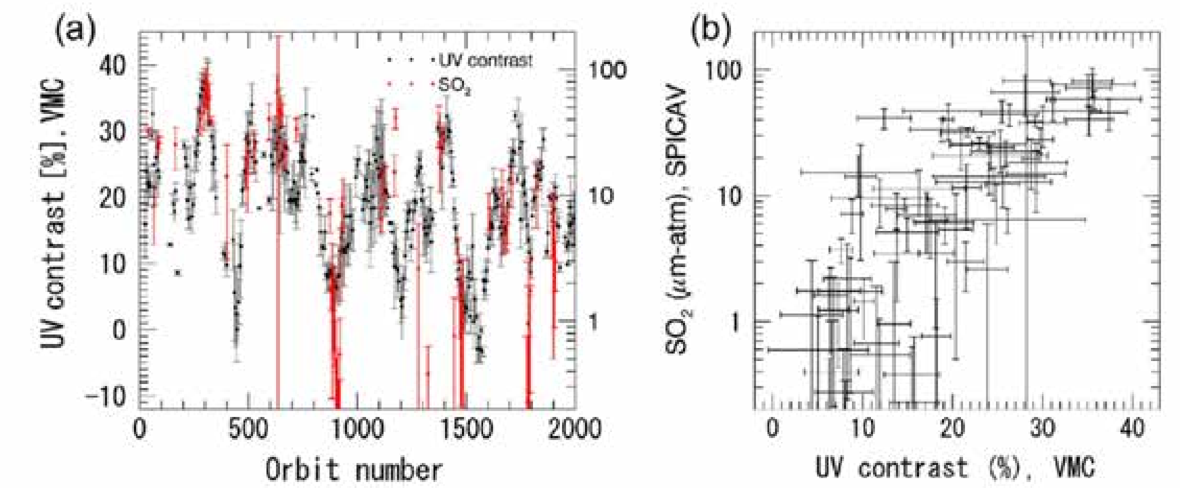

Long-term variations of the UV albedo of Venus (Lee et al. 2019)

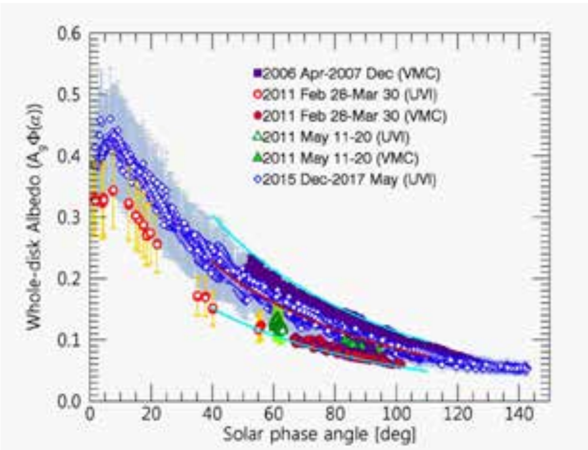

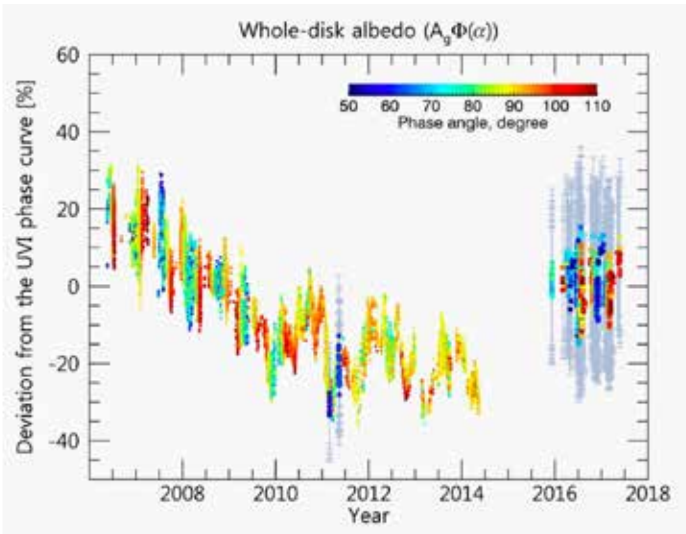

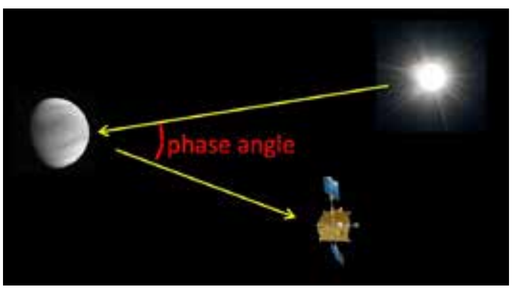

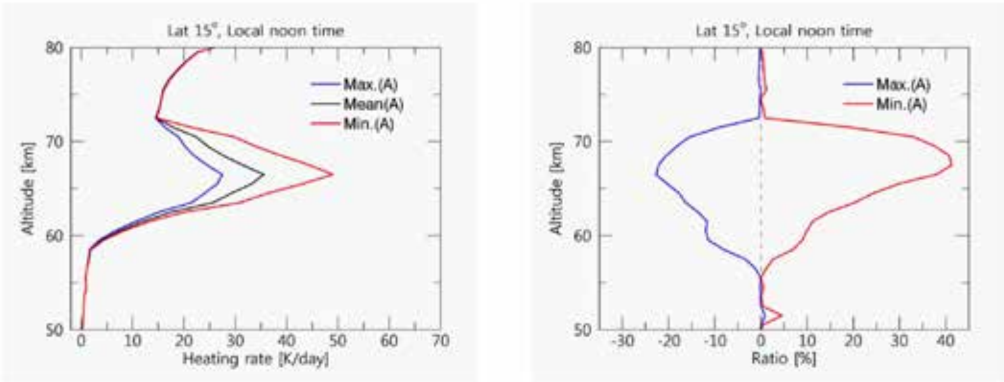

Figure 13. Calculated solar heating rate profiles for the observed maximum, minimum, and mean albedo at local noon time at 15°S. The solar heating rate is displayed in K day^{-1} (left) and as a relative ratio from the mean albedo (right).

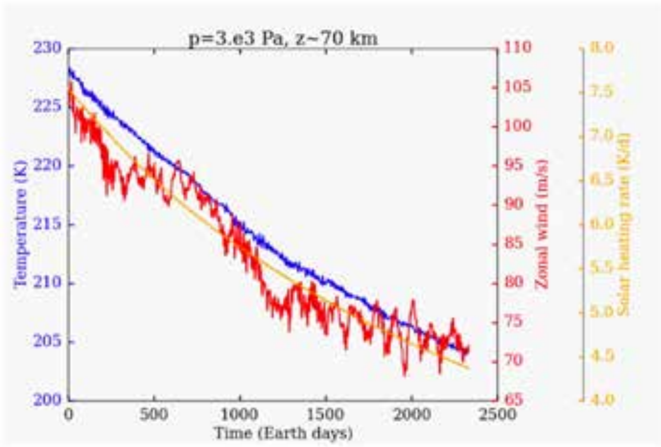

Figure 14. Temporal variations of zonal mean solar heating rate (orange), wind speed (red), and temperature (blue) at 10°S–20°S at 30 mbar (~70 km). The solar heating rate is controlled to decrease smoothly along time by 40% from the reference condition in the IPSL Venus GCM (Appendix). Simultaneous variations in temperature and zonal wind speed are shown together.

long-term variation of zonal wind in deep clouds (Peralta et al. 2018)

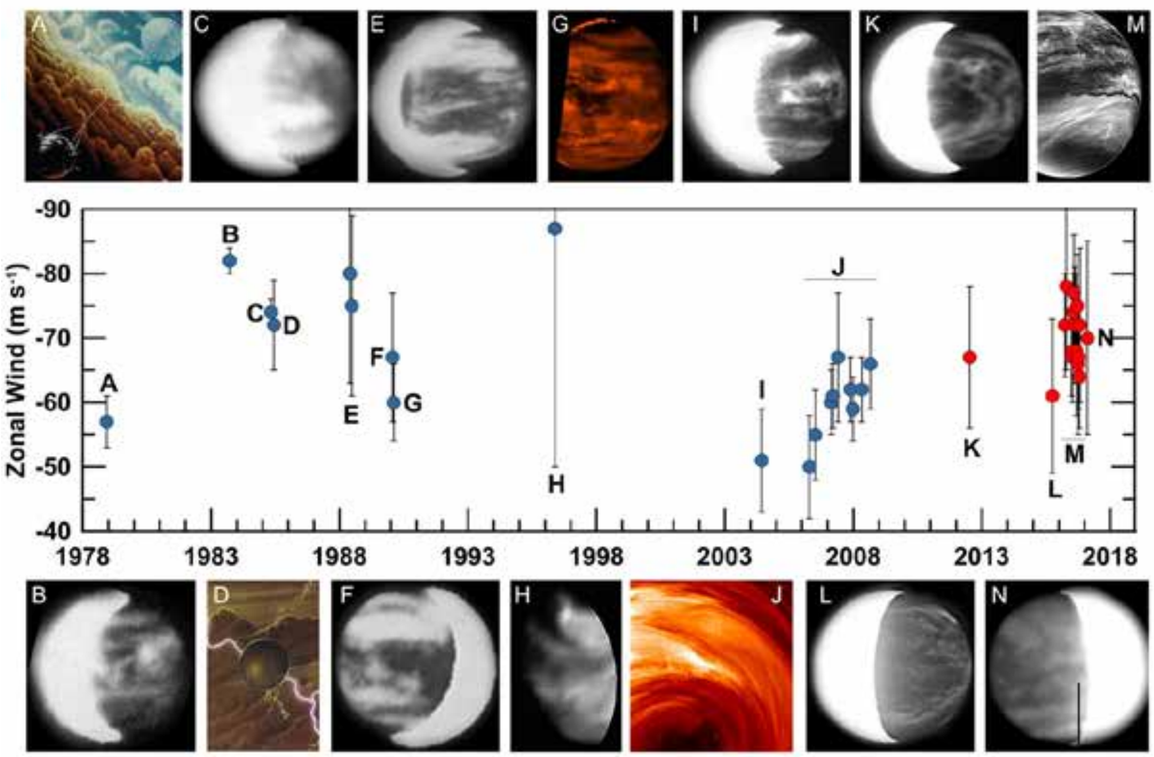

Radiative relaxation time

- Times cale of infrared cooling/solar heating
- The meridional overturning time is usually considered to be similar to the radiative relaxation time.

- Radiative relaxation time is longer for larger atmospheric heat capacities.
  - Mars : 3 Earth days
  - Earth : 100 Earth days
  - Venus : 50 Earth years

* The dynamical time scale of Venus's atmosphere can also be very long → Internal oscillation ?

Observations of exoplanets' atmospheres

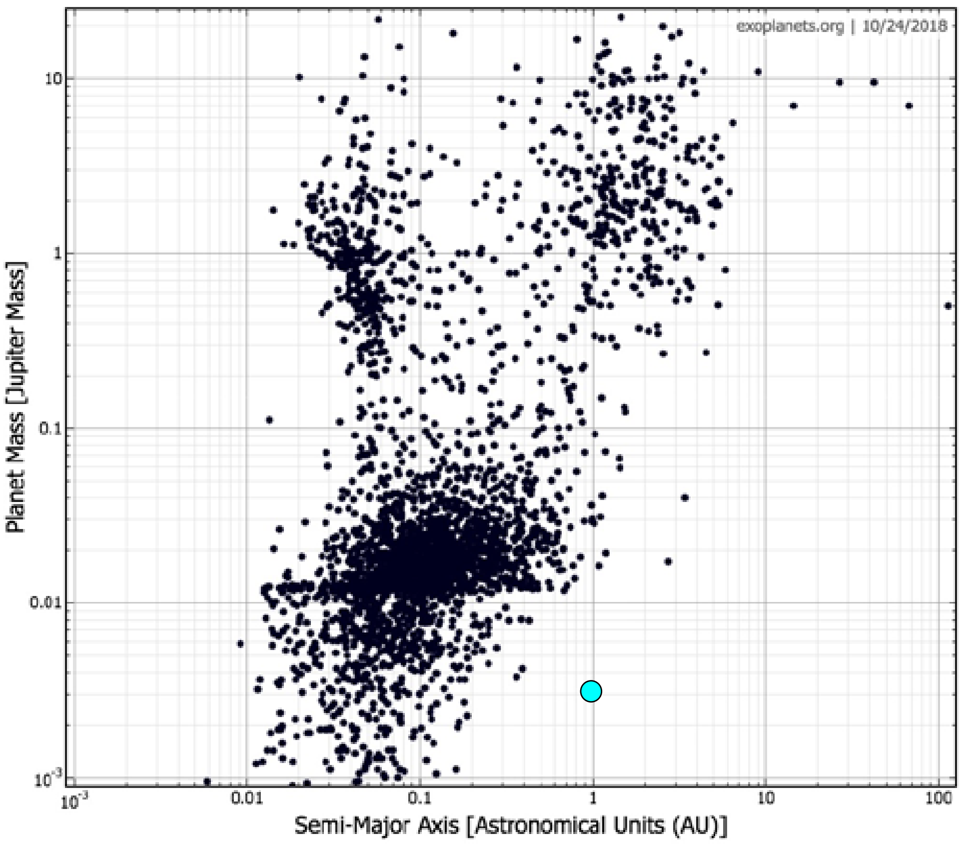

doi:10.1038/nature23266

Evans et al. (2017, Nature)

An ultrahot gas-giant exoplanet with a stratosphere

Thomas M. Evans[1], David K. Sing[1], Tiffany Kataria[2], Jayesh Goyal[1], Nikolay Nikolov[1], Hannah R. Wakeford[3], Drake Deming[4], Mark S. Marley[5], David S. Amundsen[6,7], Gilda E. Ballester[8], Joanna K. Barstow[9], Lotfi Ben-Jaffel[10], Vincent Bourrier[11], Lars A. Buchhave[12], Ofer Cohen[13], David Ehrenreich[11], Antonio García Muñoz[14], Gregory W. Henry[15], Heather Knutson[16], Panayotis Lavvas[17], Alain Lecavelier des Etangs[10], Nikole K. Lewis[18], Mercedes López-Morales[19], Avi M. Mandell[3], Jorge Sanz-Forcada[20], Pascal Tremblin[21] & Roxana Lupu[22]

- secondary eclipse of WASP-121b on 10 November 2016 using the Hubble Space Telescope (HST) Wide Field Camera 3 (WFC3)
- If upper layers are cooler than lower layers, molecular gases will produce absorption features in the planetary thermal spectrum. Conversely, if there is a stratosphere—where temperature increases with altitude—these molecular features will be observed in emission
- near-infrared thermal spectrum for the ultrahot gas giant WASP-121b, which has an equilibrium temperature of approximately 2,500 kelvin
- Water is resolved in emission, providing a detection of an exoplanet stratosphere

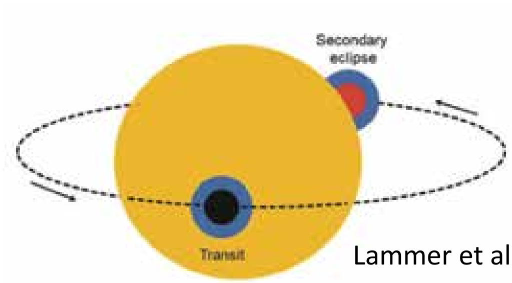

Lammer et al. (2013)

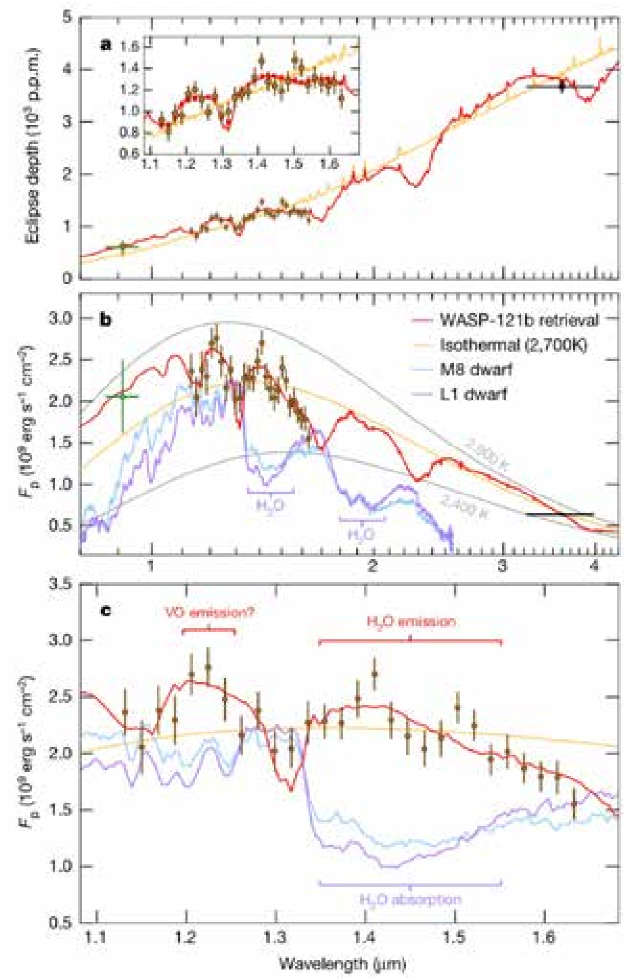

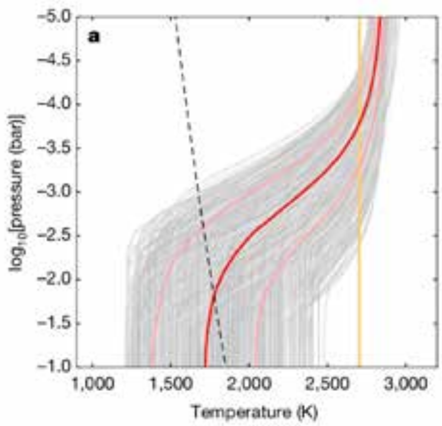

Figure 3 | Temperature–pressure profiles for WASP-121b. a, Grey lines show a random subset of *T*–*P* profiles sampled by the MCMC retrieval analysis. Red line shows the median temperature at each pressure level, and pink lines show ranges either side encompassing ±34% of the sampled profiles. Yellow line indicates the best-fit isothermal temperature of

A&A 577, A62 (2015)
DOI: 10.1051/0004-6361/201525729

Astronomy & Astrophysics

Spectrally resolved detection of sodium in the atmosphere of HD 189733b with the HARPS spectrograph*

A. Wyttenbach, D. Ehrenreich, C. Lovis, S. Udry, and F. Pepe

- high-resolution transit spectrum of HD 189733b in the region around the resonance doublet of Na I at 589 nm
- HARPS spectrograph (R = 115 000) at the ESO 3.6-m telescope
- blueshift corresponding to winds blowing at 8 ± 2 km s^{-1}

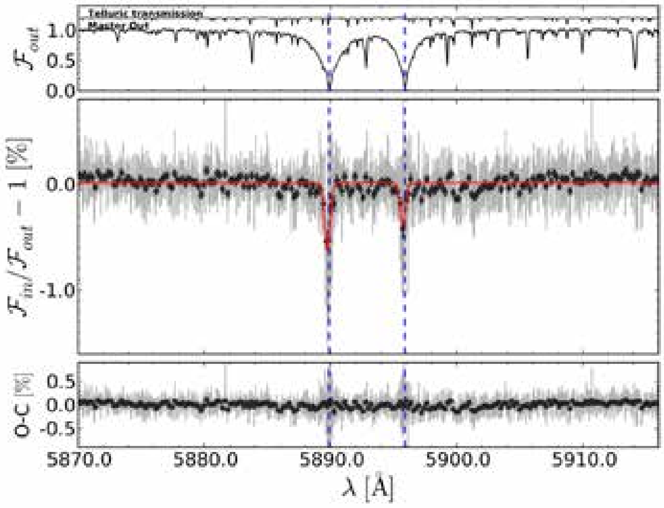

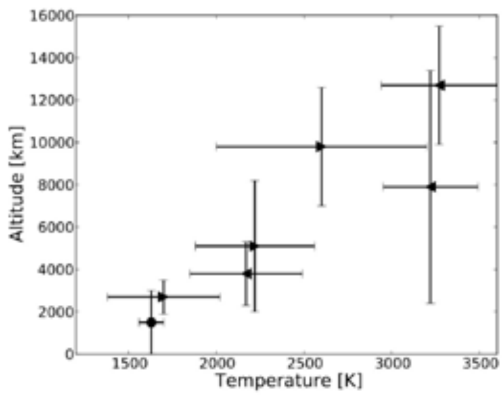

Fig. 9. Temperature profile obtained by our fitting process of η models to the transmission spectrum. The right and left triangle correspond to the Na I D1 and D2 lines. The diamond correspond to the wing shoulders. A temperature gradient of ~0.2 K km^{-1} is measured.

doi:10.1038/nature12888

Clouds in the atmosphere of the super-Earth exoplanet GJ 1214b

Kreidberg et al. (2014, Nature)

Laura Kreidberg[1], Jacob L. Bean[1], Jean-Michel Désert[2,3], Björn Benneke[4], Drake Deming[5], Kevin B. Stevenson[1], Sara Seager[4], Zachory Berta-Thompson[6,7], Andreas Seifahrt[1] & Derek Homeier[8]

- Transmission spectroscopy using Hubble Space Telescope
- We rule out cloud-free atmospheric models with compositions dominated by water, methane, carbon monoxide, nitrogen or carbon dioxide
- The planet's atmosphere must contain clouds

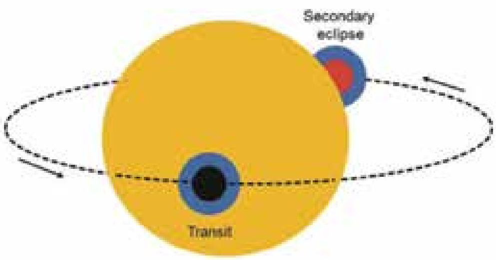

Lammer et al. (2013)

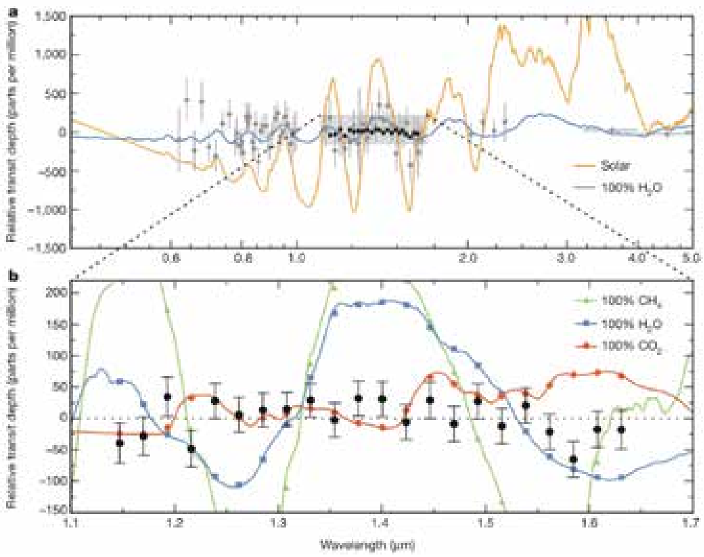

A map of the day-night contrast of the extrasolar planet HD 189733b (Knutson et al. 2007)

A minimum brightness temperature of 973 +/- 33 K and a maximum brightness temperature of 1212 +/- 11 K at a wavelength of 8 microns, indicating that energy from the irradiated dayside is efficiently redistributed throughout the atmosphere

Observed phase variation for HD 189733b, with transit and secondary eclipse visible.

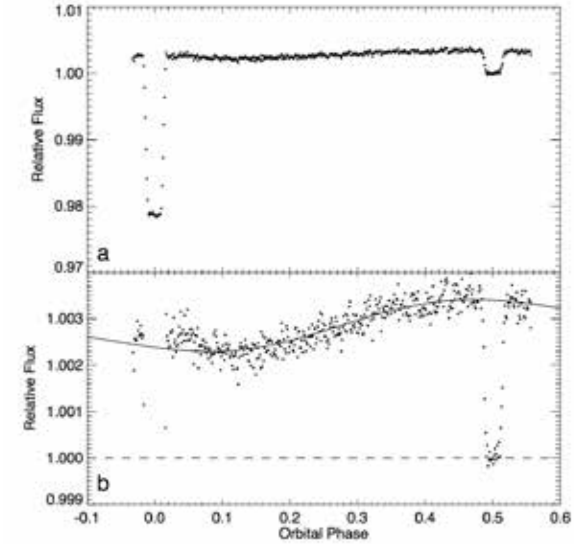

Brightness estimates for 12 longitudinal strips on the surface of the planet

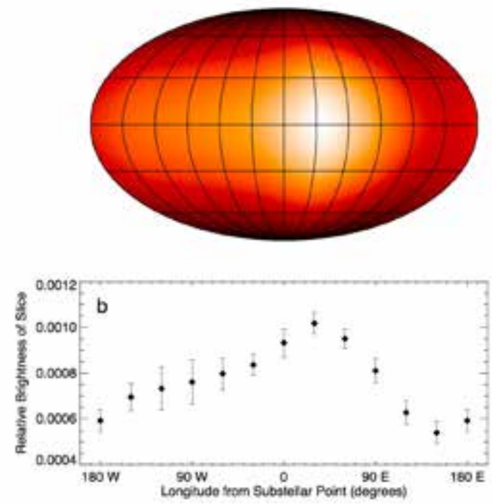

THE ASTROPHYSICAL JOURNAL LETTERS, 814:L24 (5pp), 2015 December 1 doi:10.1088/2041-8205/814/2/L24

SPATIALLY RESOLVED EASTWARD WINDS AND ROTATION OF HD 189733b

TOM LOUDEN AND PETER J. WHEATLEY
Department of Physics, University of Warwick, Coventry CV4 7AL, UK; t.m.louden@warwick.ac.uk
Received 2015 October 14; accepted 2015 November 11; published 2015 November 25

- wind velocities on opposite sides of the hot Jupiter HD 189733b by modeling sodium absorption in high-resolution transmission spectra from the High Accuracy Radial Velocity Planet Searcher

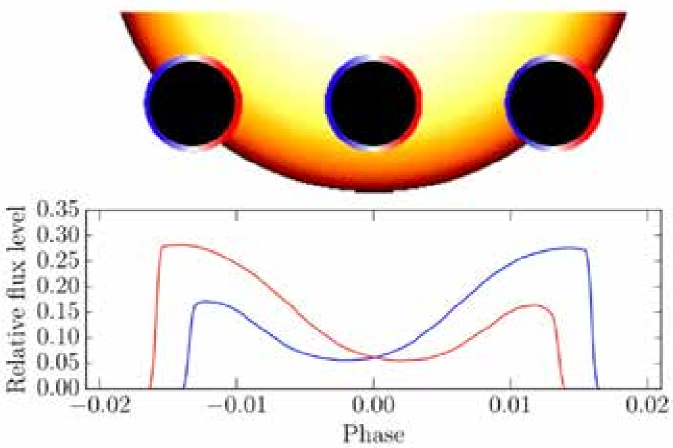

- a strong eastward motion of the atmosphere of HD 189733b, with a redshift of 2.3 km s^{-1} on the leading limb of the planet and a blueshift of 5.3 km s^{-1} on the trailing limb
- These velocities can be understood as a combination of tidally locked planetary rotation and an eastward equatorial jet, closely matching the predictions of atmospheric circulation models

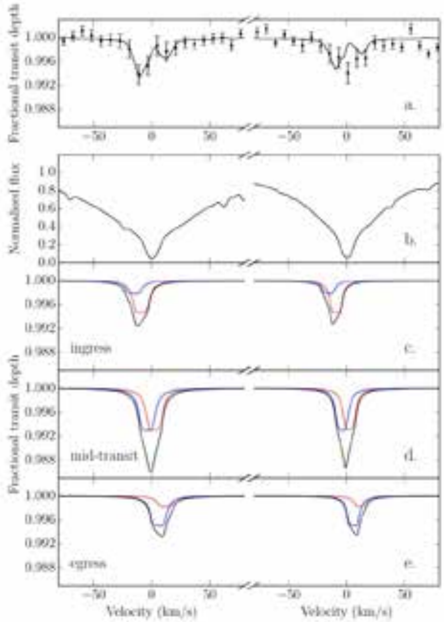

Figure 2. Planetary absorption line profiles. (a) The average sodium transmission spectrum of HD 189733b calculated in the frame of the planet (binned by a factor of 10 for clarity) with the average of our time-dependent model overlaid. The asymmetric double-peaked line profile is caused by poor cancelation of the Rossiter–McLaughlin effect in the frame of the planet (accounted for implicitly in our model). (b) The stellar sodium line profile in the frame of the star. (c)–(e) Our modeled planetary absorption line profiles in the stellar frame at ingress, mid-transit and egress respectively (with the Rossiter–McLaughlin effect removed for clarity). The contributions from the trailing (blue) and leading (red) hemispheres can be compared.

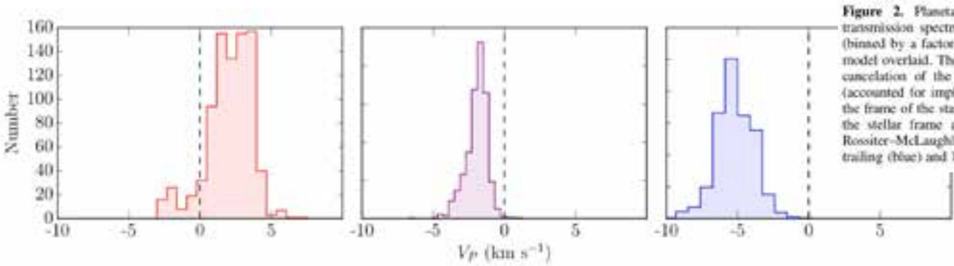

Figure 3. Posterior distributions of atmospheric velocities from our bootstrap analysis. On the leading limb of the planet (left) a red shift of $2.3^{+1.3}_{-1.5}$ km s^{-1} is found. The trailing limb is blueshifted by $5.3^{+1.0}_{-1.4}$ km s^{-1} (right). The average velocity (middle) is found to be blueshifted with a velocity of $1.9^{+0.7}_{-0.6}$ km s^{-1}. The strength and direction of the velocity offsets are consistent with a combination of tidally locked rotation and an eastward equatorial jet that is seen crossing from the dayside to the night side of the planet on the trailing limb.

Meadows et al. (2018)
ASTROBIOLOGY, Vol 18

FIG. 6. Transit transmission spectra of potential planetary environments with different O_2 abundances for planet orbiting the M5.5V star Proxima Centauri (Meadows *et al.*, 2018). Illustrating spectral features that can help distinguish photosynthetic from abiotically generated O_2 in a planetary atmosphere. From top to bottom: self-consistent Earth-like atmosphere with 50% cloud cover (21% O_2); 10 bar abiotic O_2 (95% O_2) atmosphere produced by early ocean loss with ocean remaining (purple) and desiccated (orange); 1 bar desiccated $CO_2/CO/O_2$ atmosphere that has reached a kinetic–photochemical equilibrium between the photolysis rate of CO_2 and kinetics-limited recombination (15% O_2). Effective atmospheric radius in kilometers is on the left *y* axes and transit depth is shown on the right *y* axes. The photosynthetic source for O_2 in the Earth-like case is made more likely by the presence of O_2/O_3, water, and methane. High O_2 cases with and without water are distinguished by the presence of O_4, and the behavior of the 0.5–0.7 μm Chappuis band that is sensitive to tropospheric O_3, which is more abundant in the desiccated case. The desiccated chemical equilibrium atmosphere is easily distinguished by its high levels of CO.